Performance Prediction for a Low Frequency Ultra-Wideband Synthetic Aperture Sonar

Shannon-Morgan Steele
Kraken Robotic Systems Inc.
Mount Pearl, NL, Canada
ssteele@krakenrobotics.com

Richard Charron
Kraken Robotic Systems Inc.
Mount Pearl, NL, Canada
rcharron@krakenrobotics.com

Jeremy Dillon
Kraken Robotic Systems Inc.
Mount Pearl, NL, Canada
jdillon@krakenrobotics.com

David Shea
Kraken Robotic Systems Inc.
Mount Pearl, NL, Canada
dshea@krakenrobotics.com

Abstract—**Most mine hunting missions rely on sonar imaging systems to detect and classify explosive ordnances. Traditionally, such missions employ side-looking sonar to produce acoustic images of the seabed. High frequency Synthetic Aperture Sonar (SAS) can generate range-independent, high-resolution images of the seafloor; however, these systems can suffer from high false alarm rates in cluttered environments and cannot detect buried objects due to rapid sediment attenuation. Low Frequency Synthetic Aperture Sonar (LFSAS) can penetrate the seabed and has the potential to reduce false alarm rates. By operating in the structural acoustics regime (1-50 kHz), LFSAS may be able to discriminate between man-made objects and naturally occurring seabed clutter. Ideally, an imaging system would operate in both the geometric (high frequency) and elastic regimes to maximize the probability of detecting a target. Designing and operating such an ultra-wide bandwidth sonar presents a variety of challenges in terms of optimizing and predicting sonar performance, especially in strong multipath environments. This paper will demonstrate a new model developed to predict the seabed and buried object detection performance of a Multispectral SAS under development by Kraken Robotic Systems Inc.**

Index Terms—**Synthetic Aperture Sonar, Sonar Imaging**

I. INTRODUCTION

Low Frequency Synthetic Aperture Sonar (LFSAS) is considered advantageous over high frequency SAS systems for several reasons. Lower attenuation in both the water column and sediment allows LFSAS to image and detect objects at greater burial depths and range. High frequency acoustics can only present the external or geometric shape of objects on the seafloor, making it difficult to discriminate between targets in cluttered environments. LFSAS has the potential to reduce false alarm rates and discriminate between man-made objects and naturally occurring seabed clutter by operating in the structural acoustics regime (1-50 kHz). In the structural acoustic regime objects are penetrated and resonant (elastic) modes of the target structure are excited. These resonant modes can help operators detect and identify targets. In addition to masking by clutter, explosive ordnances can be concealed through acoustic cloaking, a technique which attempts to make a target invisible over a limited range of frequencies. Acoustic cloaking can be combatted by operating over an ultra-wide bandwidth.

Sonar performance prediction modelling using the sonar equation has been well studied for a variety of different cases; however, performance prediction of a side-looking low-frequency SAS has not been well demonstrated, especially for the purpose of detecting objects buried below the seafloor. Models of the Multispectral SAS performance in various mission scenarios will be presented. Mission scenarios will include seabed and buried target detection while operating in an environment supporting a variety of multipath interference mechanisms.

II. PROTOTYPE ARRAY

The Multispectral SAS is being developed by Kraken as part of an R&D project with the Defence Research Development Canada Atlantic Research Centre. The Multispectral SAS is a fusion of several SAS systems operating concurrently at four distinct frequency bands: high frequency (140-180 kHz), mid frequency (50-90 kHz), low frequency (15-30 kHz), and very low-frequency (4-15 kHz). The system supports concurrent co-registration of all four frequency bands. The low frequency (LF) and very low frequency (VLF) bands will trigger resonant modes on objects up to 0.9 and 2.8 m, respectively. In addition to imagery, the high frequency band will also provide high-resolution bathymetry. The multispectral SAS has a modular embodiment, which allows for longer receiver apertures and high area coverage rates and has been designed to fit on medium sized towed and autonomous vehicles. The Multispectral SAS consists of 4 different transmitters and one common ultra-wideband receiver array. A hydrophone array that is multi-element in two dimensions has been selected to achieve performance gains in multipath environments.

III. PERFORMANCE PREDICTION MODEL

A. Model Development

To make the sonar equation applicable to buried object detection there are additional challenges that must be included in the model, which include sediment attenuation and sediment interface transmission. As opposed to typical buried target detection systems that look downwards, side-looking SAS geometry introduces additional factors that must be included in the sonar equation, such as multipath sources and sediment critical grazing angle. All of these corrections can be included in the model by accounting for them in the appropriate terms in the sonar equation

$$SL - TL + TS - NL + DI > DT \qquad (1)$$

where SL is the source level, TL is transmission loss, NL is noise level, DI is the directivity index, and DT is the detection threshold set by the operator, which we have set to 10 dB.

The directivity index includes both the horizontal and vertical sensitivity of a single receiver element, as the calculated SNR in (1) is for an individual element.

In the transmission loss term we account for spherical spreading and absorption in both the sediment and water column, the sediment interface transmission coefficient, and sub-bottom penetration past the critical grazing angle. The sediment interface transmission coefficient is calculated using the continuity of pressure ($T = 1 + R$), where R is the Rayleigh reflection coefficient for a given grazing angle. The transmission angle into the sediment is calculated using Snell's law. This means that once the grazing angle becomes equal to the critical angle all transmitted sound will travel horizontally along the water sediment interface. Numerous field trials have demonstrated that this behaviour is not observed in real sediments, and sediment scattering and buried targets can be detected well beyond the critical angle [1]. Not accounting for such anomalous scattering would cause us to severely under predict the VLF and LF buried target detection performance. As discussed in Appendix B-A, we have included a small-roughness perturbation model of subcritical penetration to make our sonar performance model more accurate for buried target detection.

Through the noise level term we account for ambient noise, self (electronic) noise, the multipath scenarios discussed in Appendix A, and, in the case of target detection, seabed backscatter response. The ambient noise level is estimated based on the Wenz curve [2], which is calculated using the sea state as well as the centre frequency and bandwidth of the receiver. The model used to simulate the seabed backscatter response is discussed in Appendix B-B.

In the target strength term we account for the pulse compression gain (PG) and the SAS gain (SG). It is important to note that these gains are applied differently, depending on whether the target of interest is an object or the seabed. Equation (2) is the PG applied in the case of object detection, where T is the pulse length and B is the bandwidth. In the case of the seabed, the pulse compression gain does not need to be applied because the increased echo level is exactly offset by the reduction in echo level due to the reduction in the size of the resolution cell from $\frac{CT}{2}$ to $\frac{C}{2B}$.

$$PG = 10 \log_{10}(BT) \tag{2}$$

In general, the SAS gain is defined in (3), where D is the SAS along track resolution. The SAS gain is target shape dependent. Equation (3) is appropriate for a sphere, while (4) is applicable to cylinders, where L is the length of the cylinder.

$$SG = 10 \log_{10}\left(\frac{L_{SAS}}{D}\right) \tag{3}$$

$$SG = 10 \log_{10}\left(\frac{L_{SAS}}{L}\right) \tag{4}$$

When computing the SG of a cylinder, the orientation of the cylinder should be accounted for. The orientation can be accounted for by adding a weighting term (w) to the SAS gain (5). The weighting term we have chosen is for the target strength of a finite cylinder from [3], where λ is the wavelength, d is the diameter of the cylinder, and $\beta = \frac{2\pi}{\lambda} L \sin \theta$. The angle θ depends on the along track receive position (y) relative to the cylinder and is defined in (6) as the angle with normal to the cylinder axis. Note that the model currently assumes that the long axis of the cylinder points in the across track direction.

$$w = \sum \frac{dL^2}{4} \lambda \cos^2 \theta \sin c^2 \beta \tag{5}$$

$$\theta = \tan^{-1} y \tag{6}$$

B. Simulations

This paper presents simulations of surface and buried target detection performance for the LF and VLF bands in both shallow and deep water environments. Each simulation included performance predictions in both a medium sand and silt. For all simulations the seabed was assumed to be flat (non-sloping). Spherical and cylindrical targets were simulated, with their target strength being calculated using the general simple form target strength equations in [3]. For all cylinder simulations the most difficult to detect sonar relative orientation of the cylinder was used, which is long axis pointing in the across track direction of the seafloor.

Maximum burial depths and detection ranges in the selected environments were modeled over a wide range of target diameters. For the cylinder, a diameter to length aspect ratio of 0.5 is used for all simulations. The target detection threshold for all simulations was set to 10 dB. For the maximum burial depth, the object is only considered detectable if the SNR exceeds the detection threshold for at least a 10 m interval in range.

The sonar was assumed to be mounted with a depression angle of 12 degrees. The source level terms for both the LF and VLF were set to 200 dB. The hydrophone sensitivity was measured from a prototype array to be -188 dB re V/μPa. The DI for both the transmitter and an individual element on the receiver was modeled. The pulse length is assumed to be 10 ms in deep water and 1 ms in shallow water. All simulations use a sea state of 1, wind speed of 2 knots, 10°C water temperature, 35 ppt salinity, and pH of 8.

IV. RESULTS AND DISCUSSION

A. Deep water (50 m depth, 10 m altitude)

1) Seabed Target Detection: The LF and VLF range performance for targets on the seabed is significantly further than that of high-frequency SAS systems (typically limited to 100-200 m). The surface target detection performance of both the LF and VLF is strongly dependent on the target shape and size (Fig. 1 & 2), and somewhat dependent on sediment type. In the case of the LF and VLF, the true achievable detection

range will be limited by the pulse repetition rate of the ultra-wideband system, which is chosen to ensure that the pulse-to-pulse vehicle displacement is less than half the receiver array length.
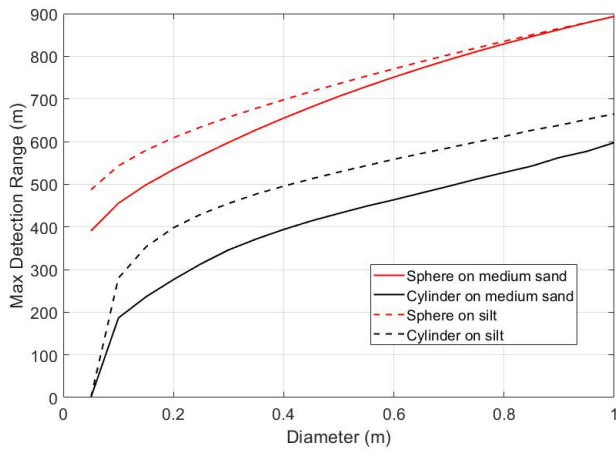
Fig. 1. LF maximum detection depth of spherical and cylindrical targets as a function of target size on the surface of a medium sand and silt.
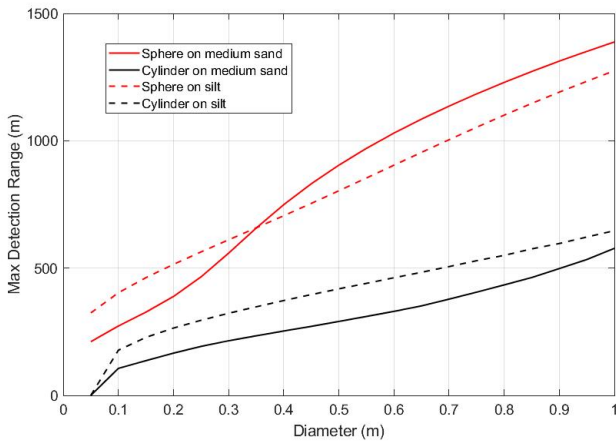
Fig. 2. VLF maximum detection depth of spherical and cylindrical targets as a function of target size on the surface of a medium sand and silt.

2) Buried Target Detection: The LF and VLF maximum buried object detection depth is also highly dependent on target shape and size, as well as sediment type (Fig. 3 & 4). Due to increased sub-bottom penetration, buried objects can be detected deeper in silt. The VLF band is able to detect objects buried almost twice as deep as can be detected by the LF band. The LF band can achieve higher resolution in angle and range (wider bandwidth), and is thus likely better suited for searching for small shallowly buried targets.

Due to sediment attenuation, sonar geometry, and the critical grazing angle in sediment, the maximum detection range of buried objects is significantly lower than surface targets (Fig. 5 & 6). In the case of surface targets, spherical objects could be detected to much further ranges than cylinders; however, when buried, cylinders can be detected much further than spheres. Buried cylinders can be detected to further ranges because they have a higher target strength, making them less affected by sediment attenuation. In most cases, the difference between the maximum buried object detection ranges of the LF and VLF is relatively low.
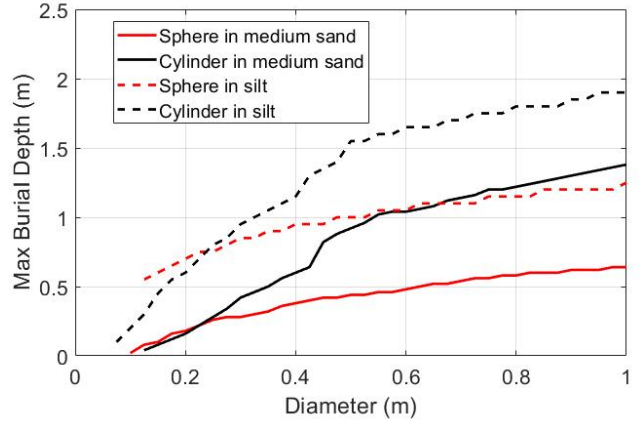
Fig. 3. LF maximum detection depth of spherical and cylindrical targets as a function of target size buried in medium sand and silt.
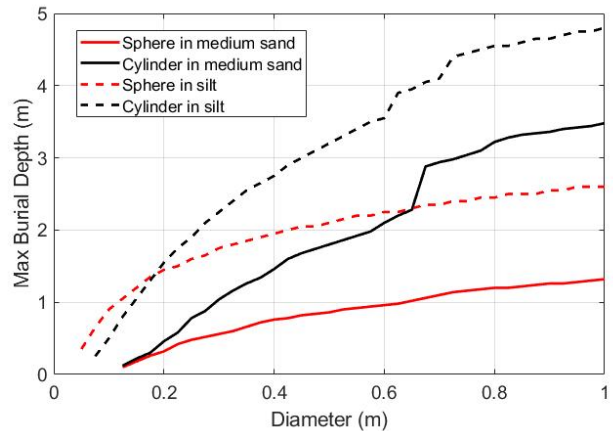
Fig. 4. VLF maximum detection depth of spherical and cylindrical targets as a function of target size buried in medium sand and silt.

B. Shallow water (10 m depth, 5 m altitude)

1) Seabed Target Detection: In shallow water, seabed target detection is strongly reduced due to the increased multipath reverberation (Fig. 7 & 8). Despite this, the model predicts that even objects 10 cm in diameter should be detectable at nearly 100 m range for both the LF and VLF.

2) Buried Target Detection: The multipath reverberation in shallow water also has a strong impact on the maximum buried object detection depth and range. The multipath interference is particularly limiting for a spherical target burried in a sediment with low sub-bottom penetration such as a medium sand (Fig. 9 & 10). In such a case the LF band performs better. The
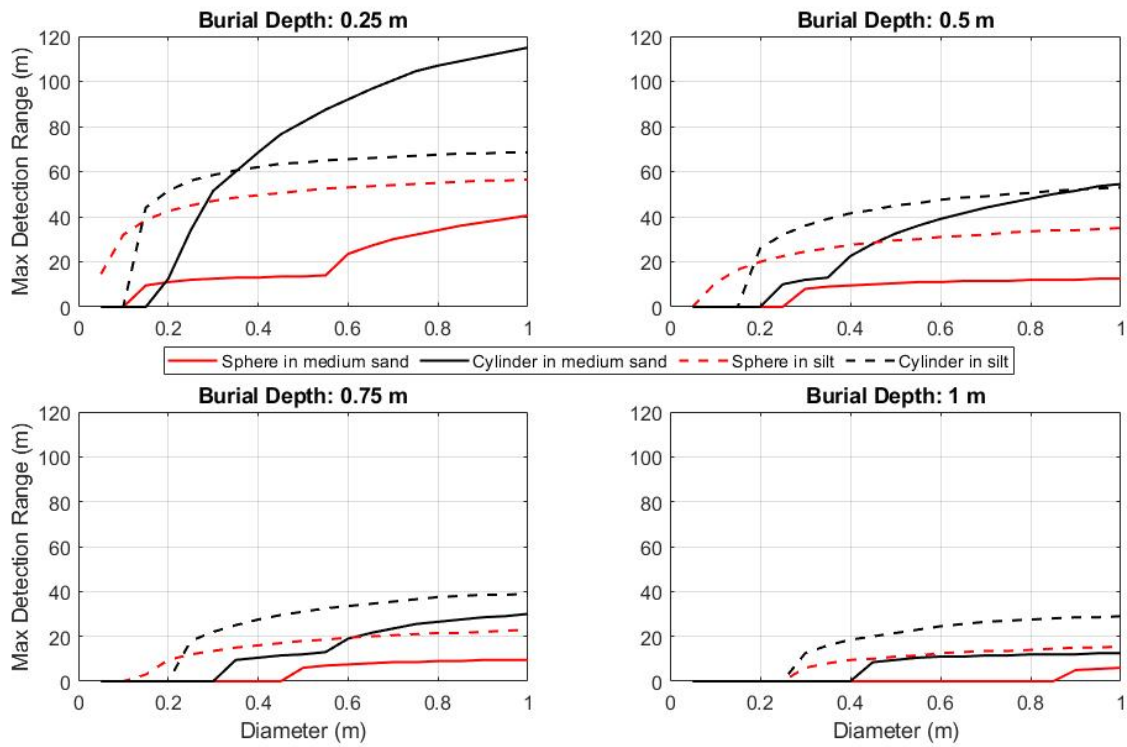
Fig. 5. LF maximum detection range of spherical and cylindrical targets as a function of target size buried at various depths in medium sand and silt.
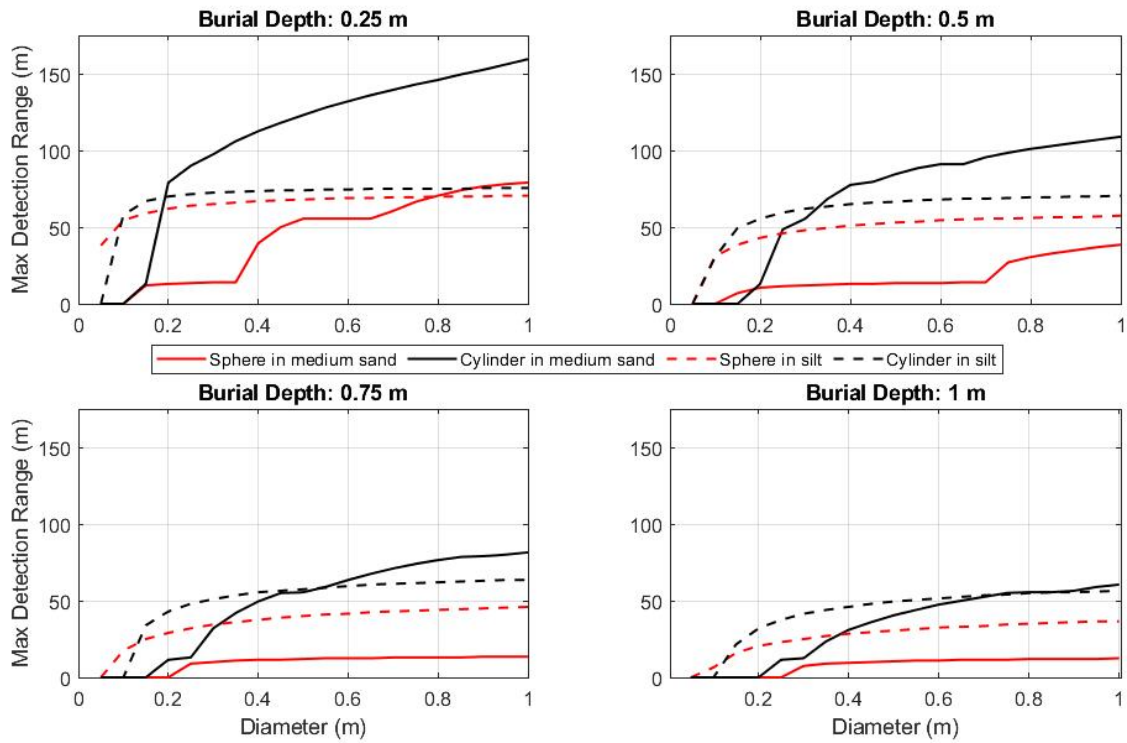
Fig. 6. VLF maximum detection range of spherical and cylindrical targets as a function of target size buried at various depths in medium sand and silt.
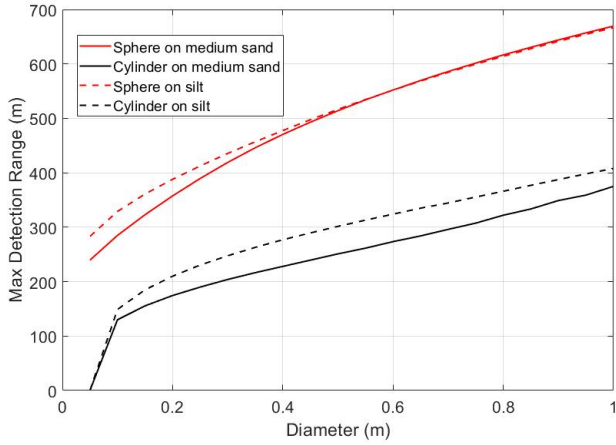
Fig. 7. LF maximum detection depth of spherical and cylindrical targets as a function of target size on the surface of a medium sand and silt.
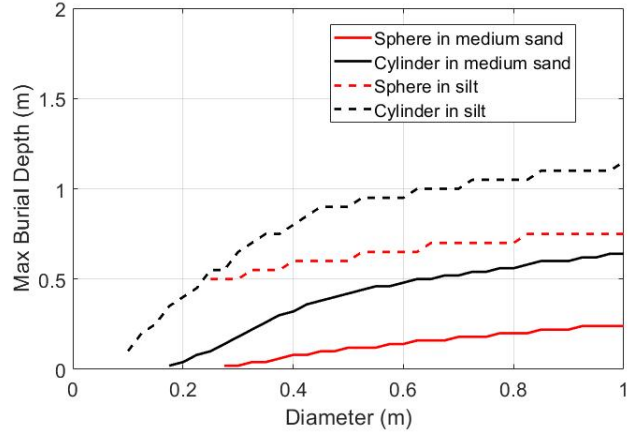
Fig. 9. LF maximum detection depth of spherical and cylindrical targets as a function of target size buried in medium sand and silt.
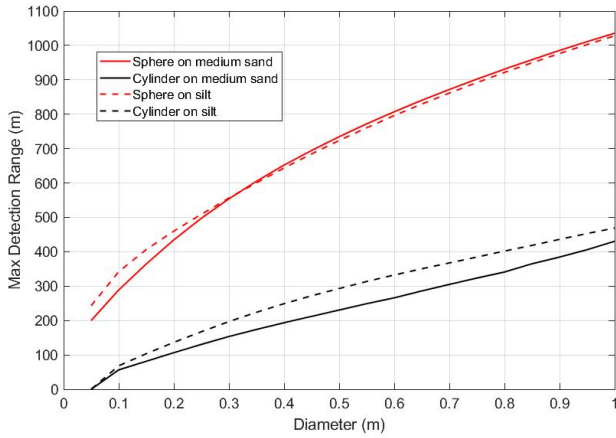
Fig. 8. VLF maximum detection depth of spherical and cylindrical targets as a function of target size on the surface of a medium sand and silt.
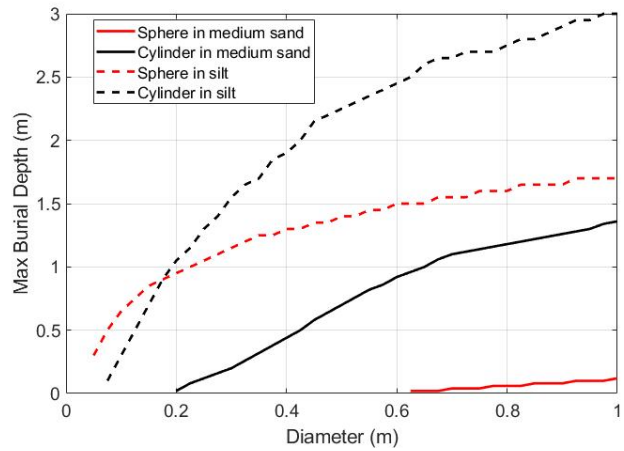
Fig. 10. VLF maximum detection depth of spherical and cylindrical targets as a function of target size buried in medium sand and silt.

multipath limits the LF and VLF buried object detection range to tens of meters or even less for small objects (Fig. 11 & 12). In many cases, the difference between the maximum buried object detection ranges of the LF and VLF is relatively low.

V. CONCLUSIONS

In this paper we introduced a new sonar performance prediction model for side-looking low frequency ultra-wideband SAS. To accurately predict performance, pulse compression and SAS gains were estimated and a model of subcritical seabed penetration was introduced.

The performance model of side-looking multi-frequency SAS demonstrates that both the LF and VLF bands of the multi-frequency SAS can be expected to image to far ranges, with the range limit ultimately being the pulse repetition rate required for SAS along track sampling. Both frequency bands should be able to detect buried targets; however, the LF band will be better suited to small shallow buried objects and the VLF band to larger and deeper buried objects. The model

demonstrates that multipath is one of the strongest limitations of the system performance, especially in shallow water, and thus multipath mitigation and rejection should be a strong priority moving forward.

APPENDIX A
MULTIPATH SCENARIOS

1) Direct sea surface return
2) From projector, to seabed, to sea surface, and back to hydrophone
3) From projector, to sea surface, to seabed, and back to hydrophone (reverse of 2)
4) From projector, to sea surface, to seabed, back to sea surface, and back to hydrophone
5) From projector, to seabed, backscattered to sea surface, reflected to seabed, and forward scattered to hydrophone
6) From projector, to seabed, forward scattered to sea surface, reflected to seabed, and backscattered to hydrophone (reverse of 5)
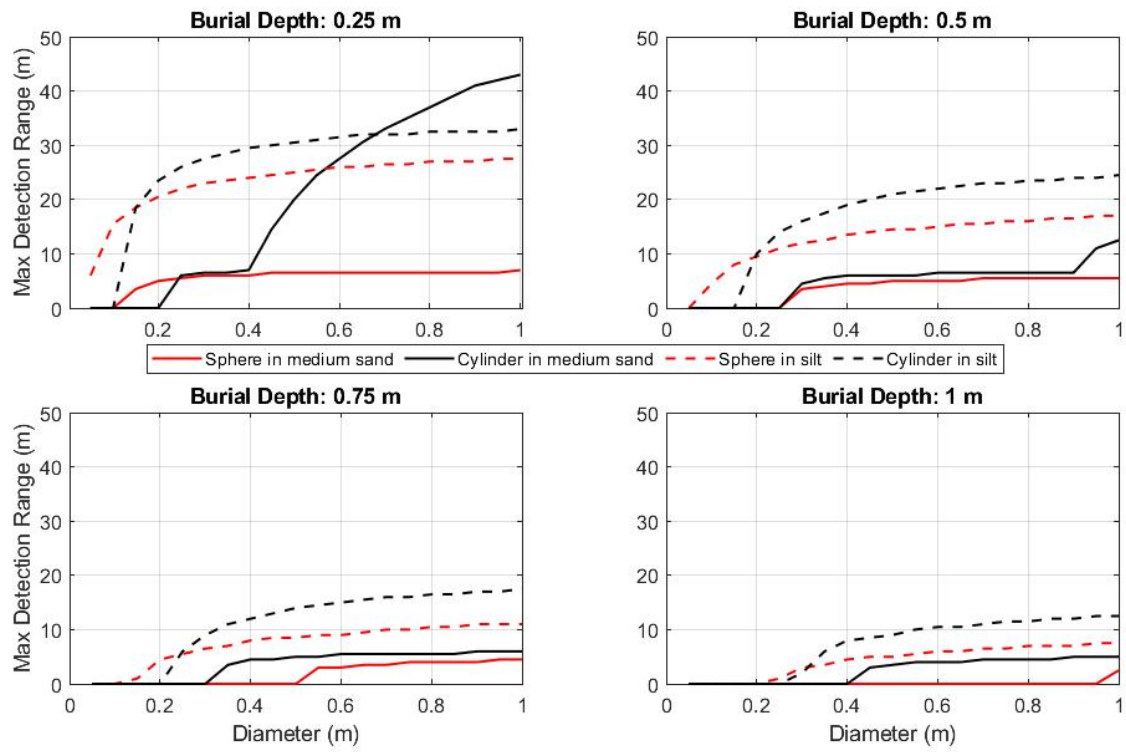
Fig. 11. LF maximum detection range of spherical and cylindrical targets as a function of target size buried at various depths in medium sand and silt.
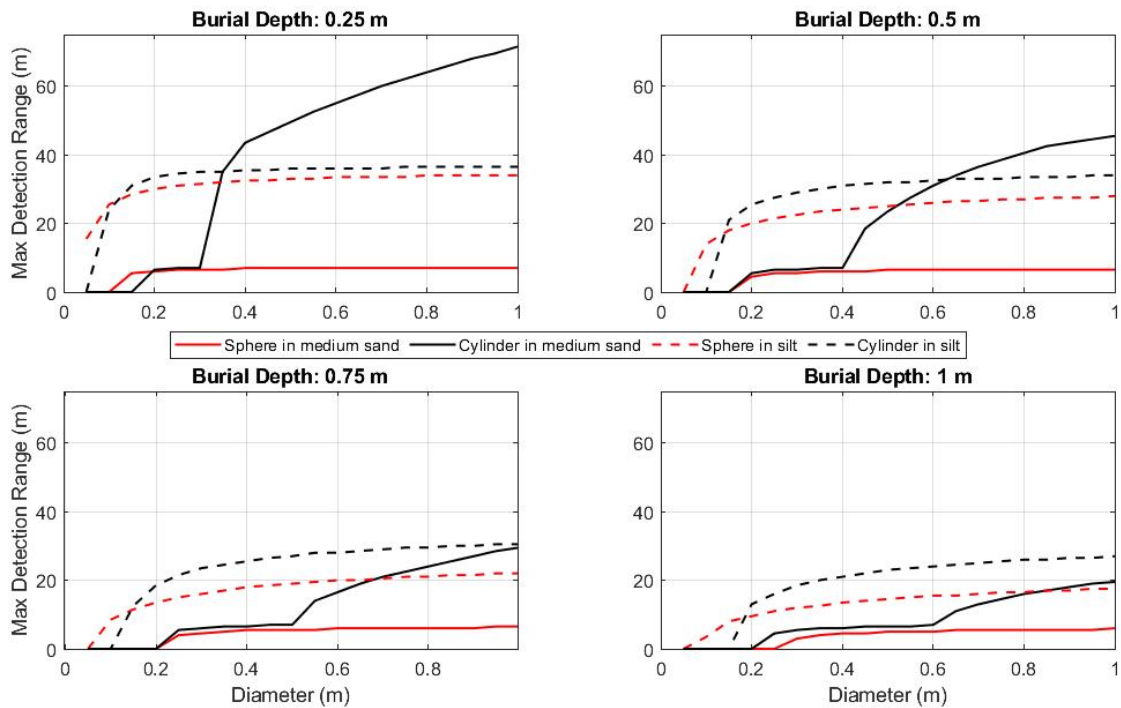
Fig. 12. VLF maximum detection range of spherical and cylindrical targets as a function of target size buried at various depths in medium sand and silt.

Appendix B
Models

A. Subcritical angle seabed penetration

At low-frequencies (less than 5 kHz) subcritical angle seabed penetration is the dominant regime for evanescent wave penetration [4]. Even the VLF frequency band just barely reaches these frequencies, and thus the evanescent wave penetration has not been included in this model. High-frequency subcritical penetration in the seabed can be due to either refraction of a Slow Wave or scattering by sediment roughness and/or sediment volume heterogeneity [1]. Due to stronger evidence towards sediment scattering being the true mechanism [4]–[6], this model will only consider subcritical penetration due to sediment roughness scattering. For the performance prediction model, we used the roughness perturbation methods described in [5], [7].

B. Elastic Seabed Bottom Backscatter

This model is an updated version [8] of the APL-UW backscattering model [9]. The model includes contributions from the sediment interface roughness and volume scattering. For roughness scattering, the model uses the small-slope formalism of [10], adapted to elastic seafloors [11], [12]. For seafloor volume scattering, the elastic perturbation approximation [13]–[15] is used. The input parameters used to generate the medium sand and silt sediments demonstrated in this paper can be found in [8].

References

[1] D. R. Jackson and M. D. Richardson, *High-Frequency Seafloor Acoustics*. Springer, 2011.

[2] G. M. Wenz, "Acoustic ambient noise in the ocean: Spectra and sources," *The Journal of the Acoustical Society of America*, vol. 34, no. 12, pp. 1936–1956, 1962.

[3] R. J. Urick, *Principles of Uncerwater Sound*. Peninsula Publishing, 2013.

[4] A. Maguer, E. Bovio, W. L. J. Fox, and H. Schmidt, "In situ estimation of sediment sound speed and critical angle," *The Journal of the Acoustical Society of America*, vol. 108, no. 3, p. 987, Oct 2000.

[5] E. I. Thorsos, D. R. Jackson, and K. L. Williams, "Modeling of subcritical penetration into sediments due to interface roughness," *The Journal of the Acoustical Society of America*, vol. 107, no. 1, pp. 263–277, Feb 2000.

[6] D. Jackson, K. Williams, E. Thorsos, and S. Kargl, "High-frequency subcritical acoustic penetration into a sandy sediment," *IEEE Journal of Oceanic Engineering*, vol. 27, no. 3, pp. 346–361, Jul 2002.

[7] J. E. Moe and D. R. Jackson, "Near-field scattering through and from a two-dimensional fluidfluid rough interface," *The Journal of the Acoustical Society of America*, vol. 103, no. 1, pp. 275–287, Jan 1998.

[8] D. Jackson, *High-Frequency Bistatic Scattering Model for Elastic Seafloors*. University of Washington Seattle Applied Physics Lab, 2000.

[9] U. of Washington, *APL-UW High-Frequency Ocean Environmental Acoustic Models Handbook*, 1994.

[10] A. G. Voronovich, "Wave scattering from rough surfaces," *Springer Series on Wave Phenomena*, 1994.

[11] T. Yang and S. L. Broschat, "Acoustic scattering from a fluid-elastic-solid interface using the small slope approximation," *The Journal of the Acoustical Society of America*, vol. 96, no. 3, pp. 1796–1804, 1994.

[12] D. Wurmser, "A manifestly reciprocal theory of scattering in the presence of elastic media," *Journal of Mathematical Physics*, vol. 37, no. 9, pp. 4434–4479, 1996.

[13] A. Ivakin, "Sound scattering by inhomogeneities of an elastic half-space," *Soviet Physics Acoustics*, vol. 36, pp. 377–380, 07 1990.

[14] A. N. Ivakin and D. R. Jackson, "Effects of shear elasticity on sea bed scattering: Numerical examples," *The Journal of the Acoustical Society of America*, vol. 103, no. 1, pp. 346–354, 1998.

[15] D. R. Jackson and A. N. Ivakin, "Scattering from elastic sea beds: First-order theory," *The Journal of the Acoustical Society of America*, vol. 103, no. 1, pp. 336–345, 1998.